ESTIMATING HIGH-RESOLUTION DIRECTIONAL CLUTTER MAPS IN FORESTED TERRAIN USING AIRBORNE LIDAR DATA

K. Clint Slatton[1,2,*], Pang-Wei Liu[2], and Heezin Lee[1]
[1] Department of Electrical and Computer Engineering
[2] Department of Civil and Coastal Engineering
University of Florida, Gainesville, FL USA 32611

Mike Campbell
US Army Topographic Engineering Center
US Army Corps of Engineers

ABSTRACT

A priori knowledge of clutter environments is critical for understanding target detection performance from airborne sensors and optimally predicting future performance to aid in mission planning. Modern airborne lidar, also known as Airborne Laser Swath Mapping (ALSM), systems can acquire decimeter scale measurements of the 3D structure in forests and urban areas. From these measurements, high resolution clutter maps that account for variations in both 3D Cartesian coordinates and viewing direction are created. Changes in the observed signal-to-noise ratio of received GPS (L-band) signals under forest canopies are correlated with a nonlinear transformation of ALSM observations to establish approximate functional descriptions of signal attenuation. The spatial support of ALSM data, segmented along lines of sight, is made wavelength dependent so that generation of clutter maps can be extended to other signals, including FM radio and TV broadcasts, as well as optical sensors.

1. INTRODUCTION

The use of unmanned aerial vehicles (UAVs) to surveil the battle space has increased dramatically in recent years. Many of the theaters that must be interrogated or monitored, however, present extremely complex clutter environments, such as urban or forested terrain. Because the clutter can attenuate and modulate targeting signals, accurate clutter maps help to reduce false alarm rates when incorporated into target detection algorithms. While clutter maps are valuable for all overhead targeting geometries, maps that account explicitly for viewing direction can be particularly valuable for targeting sensors on small low-altitude UAVs that often have limited fields of view. Clutter maps should also exhibit high spatial resolution because the available spatial resolution of many targeting sensors has increased over the past decade.

In traditional high-altitude remote sensing of the terrain where spatial resolution is at the few-meter scale or larger, forest vegetation is often modeled simply as a stratified media (isotropic in the horizontal), such that only the elevation angle (θ) between the target and the sensor governs the predicted attenuation of the targeting signal, be it emitted radiation as in thermal IR, incoherent scattered radiation as in reflected sunlight, or coherent radiation as with radar. Yet, forest researchers have long recognized that forests are anisotropic and discrete in all three dimensions. Our hypothesis is that while θ-dependencies may dominate, large variations in signal attenuation can be observed at different horizontal locations within a nominally "homogeneous" forest and that dependencies on azimuth angle (ϕ) and a targeting sensor's field of view will prove observable and important for improving detection of small or low-contrast targets.

In order to generate robust clutter maps, a high-resolution measurement of the forest structure must be made that is relatively insensitive to ephemeral conditions, such as sun angle or soil and plant moisture at the particular time the measurements are made. Furthermore, the measurements must be expressed in a three-dimensional (3D) sense in order to accommodate directionality. These constraints suggest that high-resolution lidar is well suited for making such measurements. Specifically, airborne lidar data with a high number of footprints per square meter and multiple returns per transmitted shot should prove useful for obtaining a reasonable density of returns from mid and low levels of the canopy for clutter map estimation.

For this research, a low altitude (<1000 m) Airborne Laser Swath Mapping (ALSM) system is used to obtain accurate 3D measurements of forest canopy structure at decimeter scales. GPS observations collected *in situ* are used with the ALSM data to measure the degree to which GPS signals from individual Satellite Vehicles (SVs) are

Report Documentation Page

Form Approved
OMB No. 0704-0188

1. REPORT DATE	2. REPORT TYPE	3. DATES COVERED
DEC 2008	**N/A**	**-**

4. TITLE AND SUBTITLE	5a. CONTRACT NUMBER
Estimating High-Resolution Directional Clutter Maps In Forested Terrain Using Airborne Lidar Data	5b. GRANT NUMBER
	5c. PROGRAM ELEMENT NUMBER
6. AUTHOR(S)	5d. PROJECT NUMBER
	5e. TASK NUMBER
	5f. WORK UNIT NUMBER
7. PERFORMING ORGANIZATION NAME(S) AND ADDRESS(ES) **Department of Electrical and Computer Engineering University of Florida, Gainesville, FL USA 32611**	8. PERFORMING ORGANIZATION REPORT NUMBER
9. SPONSORING/MONITORING AGENCY NAME(S) AND ADDRESS(ES)	10. SPONSOR/MONITOR'S ACRONYM(S)
	11. SPONSOR/MONITOR'S REPORT NUMBER(S)

12. DISTRIBUTION/AVAILABILITY STATEMENT
Approved for public release, distribution unlimited

13. SUPPLEMENTARY NOTES
See also ADM002187. Proceedings of the Army Science Conference (26th) Held in Orlando, Florida on 1-4 December 2008, The original document contains color images.

14. ABSTRACT

15. SUBJECT TERMS

16. SECURITY CLASSIFICATION OF:			17. LIMITATION OF ABSTRACT	18. NUMBER OF PAGES	19a. NAME OF RESPONSIBLE PERSON
a. REPORT	b. ABSTRACT	c. THIS PAGE			
unclassified	**unclassified**	**unclassified**	**UU**	**8**	

affected by forest canopy. GPS SVs provide the ability to monitor multiple L-band sources simultaneously at different azimuth and zenith angles from an observer point on the ground, allowing us to sample the forest canopy attenuation at L-band ($\lambda \approx 24\,\mathrm{cm}$) in three dimensions. We employ a methodology of statistically relating observed GPS attenuation to ALSM point cloud data, and this prediction is then used to create clutter maps at L-band. By making the support of the ALSM points used in the calculation dependent on wavelength, we can also generate clutter maps for different wavelengths, such as the radio and optical portions of the spectrum.

2. STUDY SITES AND DATA ACQUISITION

2.1 Study sites

Two forests, both located in North-Central Florida, USA, were used for this study. The topography in these sites is generally very flat, with ground elevations varying as little as 2 m. The first site is a managed pine forest, the Intensive Management Practice Assessment Center (IMPAC), established in January 1983 with two different species, loblolly pine (*Pinus taeda* L.) and slash pine (*P. elliottii* Engelm. var. *elliottii*) (Jokela and Martin, 2000). The plots in this site were designed to test the effects of understory vegetation control and fertilization on each species. The average tree height was 21.3 m and the average crown length was 6.2 m in this site. Even though the site is a managed forest, tree mortality, tree heights, the sizes of canopies, and the shapes of canopies varied significantly due to the advanced stage. Each GPS site was positioned in a different plot where the understory vegetation was controlled.

The second forest, called Hogtown forest, is a mixed coniferous and deciduous forest. The forest is composed of roughly 80% deciduous and 20% coniferous trees, but this mix varies significantly with location. Hogtown consists of trees as tall as 35 meters and possesses the characteristics expected in a natural forest where there are multiple layers of foliage, different and random spacings between trees, and significant undergrowth vegetation. Because of these multiple layers of growth, the spatial distribution of canopy foliage is a function of height as well as a function of location on the ground. Zenith-looking "fisheye" photographs of the IMPAC forest and Hogtown forest are shown in Fig. 1.

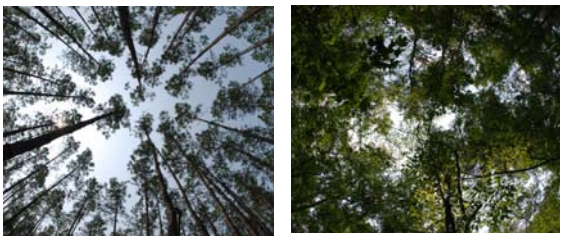

Fig. 1 An example of a zenith-oriented "fisheye" photograph of the IMPAC forest (left) and the Hogtown forest (right).

2.2 GPS measurements

Two antennas (model AT 1671-1) and two Ashtech Z-extreme (geodetic-quality) receivers are used to collect GPS data in April of 2007. One served as a clear-sky (no occlusions) base station on top of a University of Florida (UF) building (located within 10 km of both study sites), and the other served as the rover in the forests. These antennas were chosen mostly because the gain pattern for all signals between 0^o - 75^o from zenith is very uniform. In order to build a good basis of comparison between the data from the receivers, 20 minutes of calibration data was collected with the two receivers co-located on top of a UF building (i.e. clear-sky conditions).

A total of 11 locations were occupied for collecting GPS observations *in situ*: six locations at the IMPAC site and five locations at the Hogtown site. For each GPS site, the base station data and the rover data were obtained for 20 minutes. The rover antenna was mounted on a tripod at a height of 1.5 m representing the height of a hiker, soldier, or surveyor. This setup height also avoids interference from most undergrowth on the forest floor. Each GPS data set contains information from three different National Marine Electronic Association (NMEA) messages at a rate of 1 Hz. Signal-to-noise ratio (SNR) levels for each SV and position solution statistics at each site were then analyzed and compared with the base station data. These SNR values extracted from the NMEA messages were our primary measure of signal attenuation because absolute power measurements were not available from the GPS receivers.

2.3 ALSM data

The ALSM data was collected in February and March of 2006 by the UF ALSM system. Collection of GPS data and ALSM data in the same year and season is ideal, but in many cases canopy changes will be moderate to negligible if measurements are taken during the same season and separated by only a few years. This is particularly true for warm southern US forests that exhibit minimal leaf drop and that have experienced no recent disturbances. The ALSM data sets were collected from a

commercially manufactured (Optech, Inc.) lidar mounted on a Cessna 337 aircraft. The Nd:YAG laser operates at a 1064 nm wavelength (near-IR) with a laser pulse rate of 33 kHz, and the sensor records the first and last return pulses from each transmitted pulse. The Hogtown site was acquired with typical flight parameters with an average height of 600 m above ground level (AGL), scan rate of 30 Hz, and a scan angle range of ±20°. The IMPAC site was flown for a special project that required higher than normal point densities, so an average height of 350 m AGL and a scan angle range of ±10° were used. In both cases, adjacent parallel swaths were overlapped by 50%. The resulting average point densities over the study sites were 20.8 points/m^2 for IMPAC and 3.9 points/m^2 for Hogtown.

3. METHODS

When modeling microwave signaling performance, it is critical to consider the region around the line of sight in which the signal is severely impacted by diffraction, absorption, and scattering caused by the presence of objects and occlusions. For this work, we employed the concept known as a Fresnel zone for this purpose. A Fresnel zone surrounding the visual line-of-sight (LOS) between a transmitter (Tx) and a receiver (Rx), as shown in Fig. 2, defines a circular aperture with respect to location between Tx and Rx. Objects inside that aperture are considered to have a potentially significant impact on the signaling performance. The general equation is defined as

$$F_n = \sqrt{\frac{n\lambda d_1 d_2}{d_1 + d_2}} \qquad (1)$$

where, F_n is the n^{th} Fresnel zone radius at the location of object P, d_1 is the distance of P from the transmitter, d_2 is the distance of P from the receiver end, and λ is wavelength of the transmitted signal (all are in meters). From (1), we see that the longer the wavelength is the larger the Fresnel zone, and the largest cross section radius of the n^{th} Fresnel zone, $F_{n,\max}$, occurs at the midpoint ($d_1 = d_2$). For this work, we consider only the 1st order Fresnel zone and therefore let n=1. It is worth noting that there is no explicit notion of object size in the Fresnel zone formulation.

We define a LOS vector centered at the GPS antenna and aimed at a particular SV (Fig. 3), and then use the Fresnel zone to define a spatial neighborhood in which lidar returns are from objects likely to affect the SNR of the GPS signal. We compute the number of ALSM points falling inside this zone and use that as a measure of the density of foliage in the primary signal path. So that we only use the ALSM points corresponding to the above-ground biomass, an adaptive multiscale filter developed by Kampa and Slatton (2004) is employed to segment ground from non-ground lidar returns. The ALSM point densities in the Fresnel zone were then compared to the SNR levels of each SV.

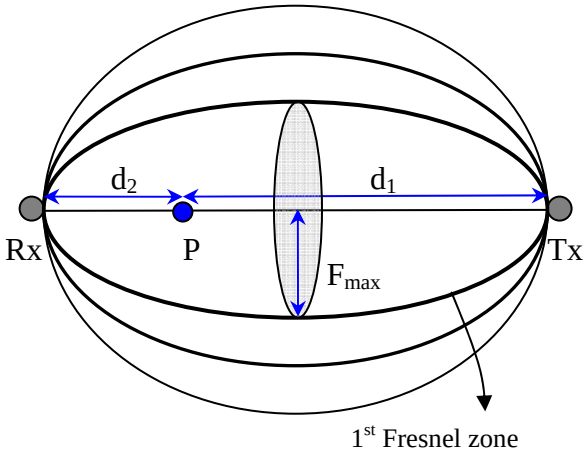

Fig. 2 A diagram of Fresnel zones (n=1, 2, 3) between a transmitter (Tx) and receiver (Rx). Each Fresnel zone is approximately ellipsoidal in shape. Objects (denoted by "P") may affect the signal if inside a Fresnel zone. The lower the Fresnel zone number, the more likely an interior object will have an effect.

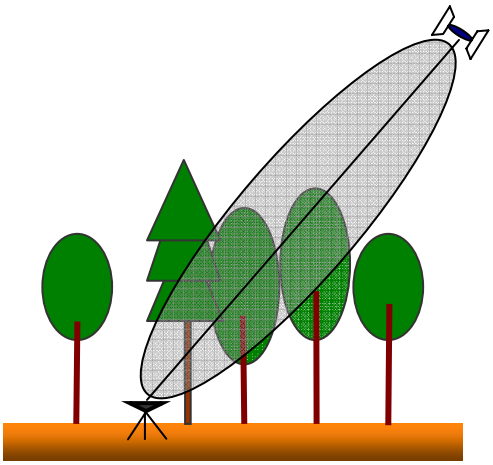

Fig. 3 The first Fresnel zone shown between a GPS satellite and the receiver in a forest.

We naturally expect that the higher the point density in the Fresnel zone, the more attenuation of the microwave signal. Yet, an object's location within the Fresnel zone should also affect its ability to perturb the signal. Thus, a weighting function based on both the distance between the ALSM point and the receiver antenna and the angular divergence from the point to the

visual LOS is considered here. For the distance weighting w_d, points located farther from the antenna are assigned lower weight, requiring the function decrease monotonically with the distance as indicated by

$$w_d = \frac{(d - d_{vanishing})^2}{d_{vanishing}^2} \quad (2)$$

where, d is the point distance from the antenna, and $d_{\text{vanishing}}$ is the distance threshold from the ground-based observer where occluding medium ends (based on slant path and maximal canopy height, such that $d_{\text{vanishing}} > \max(d)$ (Lee *et al.*, 2008). The mapping in (2) is non-linear because moving a point along the LOS a fixed distance will have more impact close to the observer than far away from the observer. A function w_ρ is defined as in equation (3) for the divergence weighting requiring the function decreases exponentially from a maximum value at the LOS vector as a function of the divergence angle ρ to a minimum value at the boundary of the Fresnel zone, where ρ_0 is the divergence angle at the boundary of the Fresnel zone.

$$w_\rho = \exp(-\rho/\rho_0) \quad (3)$$

Regression is performed to characterize the observed GPS signal attenuation, taking the weighted ALSM point densities as the explanatory variable and the signal loss ratio (SLR) as the response variable. SLR is defined as the ratio of the difference between the base station SNR (SNR_{base}) and the rover SNR (SNR_{rover}) to the base station SNR, lying on the interval [0, 1], as in (4).

$$SLR = \frac{SNR_{base} - SNR_{rover}}{SNR_{base}} \quad (4)$$

To establish an approximate functional description of the observed signal attenuation, both a conventional Beer's Law model and modified exponential decay (MED) model developed by the International Telecommunication Union (ITU) for microwave signals in vegetation (Savage and Ndzi, 2003) are employed. As described in Wright *et al*. (2008), we simplified the Beer's Law model as in (5) and the MED model as in (6). In those equations, *L* is the absorption coefficient, *d* is the path length in the medium, and *A*, *B*, and *Z* are parameters that need to be estimated from the observations.

$$L = Bd \quad (5)$$

$$L = Ad^Z \quad (6)$$

Once the parameters are estimated from the regression, since the measurements are expressed in 3D, high-resolution 3D clutter maps are generated by locating one end of the Fresnel zone at each pixel in the region of interest (ROI) and terminating it at the location of a hypothetical targeting sensor. The set of lidar points in the Fresnel zone at a pixel is weighted according to (2) and (3), and denoted by S_i. The relative clutter value $C(x, y)$ in the clutter maps are then estimated by normalizing S_i contained in each Fresnel zone to lie on the interval [0, 1].

4. RESULTS

4.1 Estimated model

Since our microwave sources (GPS satellites) are moving, we needed to define a compound Fresnel zone to encompass the arc of the SVs across the sky. We selected the central 10 minutes of each 20 min GPS recording epoch, and defined a compound Fresnel zone based on the two end points of the arc. As a result, cone-like scope function originating at the GPS antenna with a radius of approximately 4.5 m at the canopy top was defined for each SV at all GPS sites recorded in both sites. The set of ALSM points S_i inside this scope function were then used to fit the Beer's Law and MED models. Data dropouts (zero readings in the NMEA message due to severe occlusion) were counted,. In practice, the degradation of the static position solutions by the presence of a significant number of SV dropouts, is mitigated by averaging over ten minute epochs.

We plot the SLR between the base station and the rover data for each SV versus weighted ALSM point density in IMPAC and Hogtown by fitting Beer's model and MED model in Fig. 4. We see that the IMPAC forest gives a much closer fit than Hogtown to both the Beer's Law model and the MED model. This is because, overall, the vegetation distribution in Hogtown is more irregular than in the managed IMPAC forest. However, it is worth noting the two data points in Fig. 4 (red ellipse) that affect the parameters in the equation substantially. The SLRs of these points are very small even though the weighted point densities are relatively high. It is suspected that the received signals are strengthened because of the reflected signals from very close tree trunks (i.e. multipath). When these two points at Hogtown are omitted, we obtain some improvement in the correlation coefficients: $R^2 = 0.4516$ for Beer's model and $R^2 = 0.4296$ for MED model.

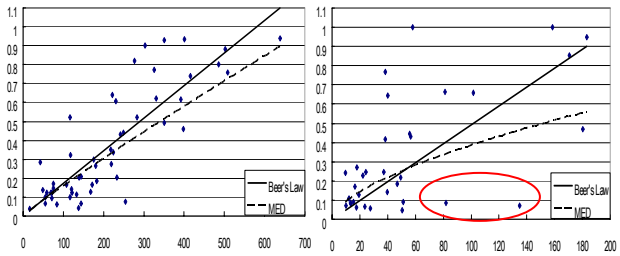

Fig. 4 SLR of each SV plotted against the weighted ALSM point density inside the Fresnel zone for IMPAC (left) and Hogtown (right) using the Beer's Law model (solid line) and the MED model (dotted line). The estimated model equation for IMPAC is Y = 0.0017X, R^2 = 0.7134, RMSE = 0.1535 for the Beer's Law model, and Y = 0.0022×$X^{0.9293}$, R^2 = 0.6122, RMSE = 0.1681 for the MED model. The estimated model equation for Hogtown is Y = 0.0049X, R^2 = 0.3061, RMSE = 0.2501 for the Beer's Law model, and Y = 0.0227×$X^{0.6154}$, R^2 = 0.3025, RMSE = 0.2528 for the MED model.

4.2 Clutter maps

Given the spatially explicit setup of our model, a clutter map can be generated for an assumed L-band source. For illustrative purposes, we select the case where the Beer's Law model is used at Hogtown for our estimated model to create the map (see Fig. 5). We assume a hypothetical airborne sensor flies 250 m south of the center location, at an elevation of 500 m. We compute weighted ALSM point densities inside the compound Fresnel zone for each 1m × 1m pixel in the map, directed at the source.

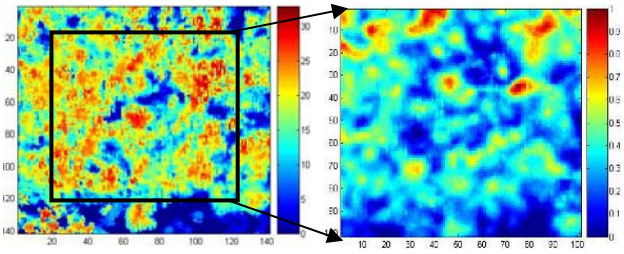

Fig. 5 Clutter map result over Hogtown. (Left) A 100 m × 100 m area (box) is selected from an image of above-ground canopy heights derived from the ALSM data, with 1m × 1m pixel sizes. Axes and color bar units are in meters. (Right) corresponding L-band clutter map [0,1] for a sensor 250 m south of the center and 500 m high. Axes units in meters.

We expect the effects of clutter to depend on the wavelength of the sensor since the size of the Fresnel zone is a function of the wavelength of the transmitted signal. With the same estimated model, two clutter maps with different wavelengths are presented in Fig. 6. First, a clutter map for an optical sensor, such as a multispectral imager, is shown. Next, a clutter map perceived by a ground-based receiver of very high frequency (VHF) radio waves, (e.g. FM radio or TV broadcasting) is shown. As expected, the longer wavelengths of the radio signals result in a spatially smoother image. The case of L-band microwave signals (λ = 0.2 m) is in between these two.

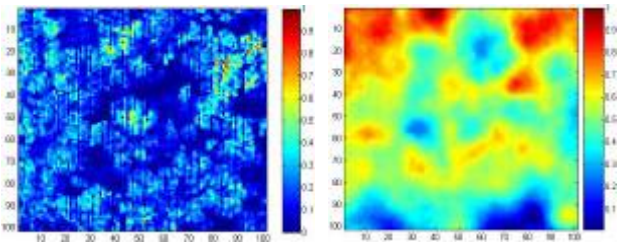

Fig. 6 Clutter maps of the same area in Fig. 5 for two different cases. (Left) Optical sensor (λ = 1 μm), and (Right) radio sensor (λ = 2.78 m). Axes labels are in meters.

4.3 Attenuation maps

A 1st order model which counts only signal attenuation through the medium, ignoring scattering and multipath effects, can be used to evaluate the detectability of targets under forests given the ALSM-derived clutter maps. Monostatic "radar equation" power relations from Ulaby *et al.*, (1986) are simplified for this case and employed, along with our SLR, for the situation depicted in Fig. 7, as shown in (7), (8), and (9)

$$P_r = \frac{P_s}{4\pi R^2} \cdot G_s \tag{7}$$

$$P_t = P_r \cdot \sigma \approx P_r \cdot (A_{rs} \cdot (1 - f_a) \cdot G_t) \tag{8}$$

$$P_E = \frac{P_t}{4\pi R^2} \cdot A_r \tag{9}$$

where, P_s is the transmitted signal power from an airborne source, such as a radar, P_r is the incident power per unit area on the ground-based target, P_t is the power re-emitted from the target, P_E is the power at the receiver reflected from the target, G_s is the transmitter antenna gain in the direction of the target, G_t is the gain at the target in the direction of the source, f_a is the fraction of the incident power absorbed by the target, A_{rs} is effective receiving area of the target, A_r is effective receiving antenna area, and R is the distance between the sensor and the target. Since the vegetation medium between the sensor and the target attenuates the signal power, (7) can be modified as

$$P_r = \frac{P_s}{4\pi R^2} \cdot G_s \cdot (1 - SLR) \quad (10)$$

These equations can be simplified by assuming the effective areas A_{rs}, A_r are the same size as the pixel size (i.e. A_{rs}, A_r =1). Both gain parameters G_s, G_t are set to 0.9 assuming that 90% of the power is in the direction of the receiver and target, and this value is applied to the entire ROI (here, 100 m × 100 m) since most radars have wide beams. The fraction of the absorbed power f_a is also simplified by arbitrarily setting it to 0.3 for metal targets and 0.6 for the ground since metal targets typically re-emit microwave signals more efficiently than the ground. The received power at the radar can then be written as

$$P_E = \left(\frac{1}{4\pi R^2}\right)^2 \cdot (0.9)^2 \cdot (1 - f_a) \cdot (1 - SLR)^2 \cdot P_s \quad (11)$$

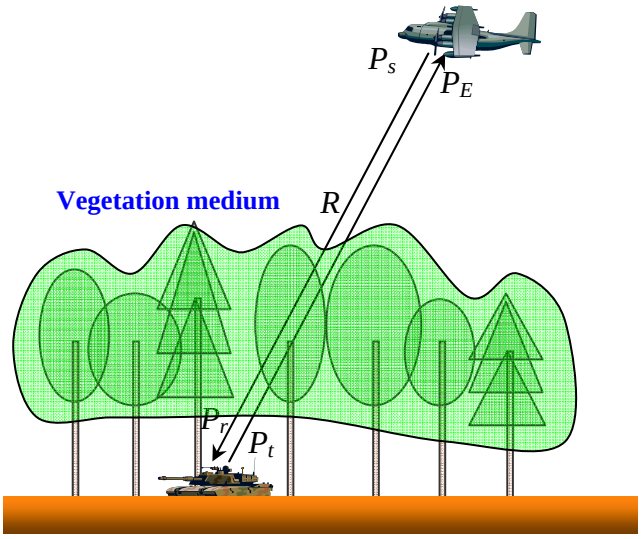

Fig. 7 A diagram showing the transmitted signal and received signal through the vegetation medium. The attenuation by the vegetation medium is approximated by SLR, and is squared due to the two-way path.

As an example, we simulated a case where two 4 m × 5 m metal targets are deployed in the area of Hogtown forest shown in Fig. 5; one in an open space (T_1) and the other one under heavy vegetation (T_2), as shown in Fig. 8. The received L-band signal from each pixel location is shown in the right figure, assuming that the signal is reflected from either the ground or the targets (i.e. no direct backscatter from the vegetation). Speckle effects are also ignored. The hypothetical targeting sensor was flying at 500 m AGL and 250 m south from the center of the area, and the transmitted signal power P_s was specified to be 50 W. The received power P_E was 1.44×10^{-12} W from T_1 and 7.76×10^{-13} W from T_2. Albeit that the true physics of the interactions between the radar signal and the environment are approximated, we nonetheless obtain a useful attenuation map that clearly depicts the differences in target visibility due to occluding vegetation.

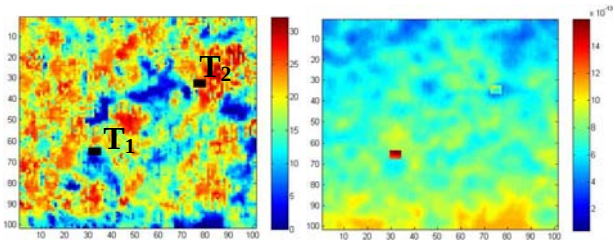

Fig. 8 Attenuation map for area shown in Fig. 5 with two hypothetical ground targets (T_1 and T_2). (Left) the locations of two metal targets overlaid on an image of tree heights. (Right) received signal power (in watts) at the airborne L-band radar from the ROI assuming P_s = 50 W.

4.4 Detectability along a flight path

Since targeting sensors are often airborne, they move along a flight path. Therefore, consecutive maps of the received power at the receiver P_E can be derived by changing the azimuth and/or zenith angles. In Fig. 9, the azimuth angle varies from 120 ^{o} to 240 ^{o} as a hypothetical sensor flies by the ROI. The received signal is generally expected to be stronger at the azimuth angle ϕ = 180 ^{o} because of the shorter distance between the targets and the sensor. This was the case for T_1 as shown in the 4th map from the bottom row of attenuation maps. However, the 3rd map shows the strongest received signal for T_2, P_E = 9.36×10^{-13} W, which is higher than P_E in the 4th map. This is not surprising because the tree height image indicates less vegetation on the lower left side of T_2.

5. CONCLUSIONS

In this study, we developed a method for estimating L-band signal attenuation in a spatially explicit and directional fashion in forests using *in situ* GPS and ALSM observations. The Fresnel zone concept was employed to determine the density of foliage along the primary signal path as a function of the number of ALSM points inside this zone and allowed the extension of the predictions to other wavelengths. Roughly equivalent results were obtained based on Beer's Law and the MED model. Regression residuals for Hogtown were worse than from IMPAC, suggesting that the higher ALSM point density at IMPAC better captured important foliage structure.

The modeling approach used here was necessarily approximate because we desire only to capture the 1st order physics so that a minimum number of parameters must be specified or learned from the data. The motivation for this approach is to maintain straightforward generalization to other forest types. A more sophisticated model, that includes vegetation backscattering and multipath could better describe the 3D L-band attenuation, but would necessarily be harder to apply to non-training locations because of the greater knowledge of the vegetation required. We demonstrated that once a spatially explicit model for signal loss is developed, high resolution (1m × 1m) 2D clutter and attenuation maps can be generated that should be quite useful for mission planning for airborne sensors.

ACKNOWLEDGMENTS

This work was partially supported by the National Science Foundation (NSF) through the National Center for Airborne Laser Mapping (NCALM) under grant EAR-0518962 and the US Army Research Office (ARO) under grant W911NF-06-1-0459. We are grateful for the assistance of the Forest Biology Research Cooperative (FBRC) in providing access to the experimental IMPAC study site.

6. REFERENCES

Jokela, E.J. and Martin, T.A., 2000: Effects of Ontogeny and Soil Nutrient Supply on Production, Allocation, and Leaf Area Efficiency in Loblolly and Slash Pine Stands, *Canadian Journal of Forest Research*, **30**, 1511-1524.

Kampa, K. and Slatton, K.C., 2004: An Adaptive Multiscale Filter for Segmenting Vegetation in ALSM Data, *Proc. IEEE 2004 International Geoscience and Remote Sensing Symposium (IGARSS)*, **6**, 3837-3840.

Lee, H., Slatton, K.C., Roth, B.E. and Cropper, W.P.: Prediction of Forest Canopy Light Interception Using Three-Dimensional Airborne LiDAR Data, *International Journal of Remote Sensing*, doi: 10.1080/01431160802261171, (in press), 2008.

Savage, N. and Ndzi, D., 2003: Radio Wave Propagation through Vegetation: Factors Influencing Signal Attenuation, *Radio Science*, **38-5**, ISSN 0048-6604.

Ulaby, F.T., Moore, R.K. and Fung, A.K., 1986: Microwave Remote Sensing: Active and Passive-Volume III: From Theory to Application, Artech House, MA, USA

Wright, W.C., Liu, P.W., Slatton, K.C., Shrestha, R.L., Carter, W.E. and Lee, H., 2008: Predicting L-Band Microwave Attenuation through Forest Canopy Using Directional Structuring Elements and Airborne Lidar, *Proc. IEEE International Geoscience and Remote Sensing Symposium (IGARSS)*, Boston, USA, 7-11. (*in press*)

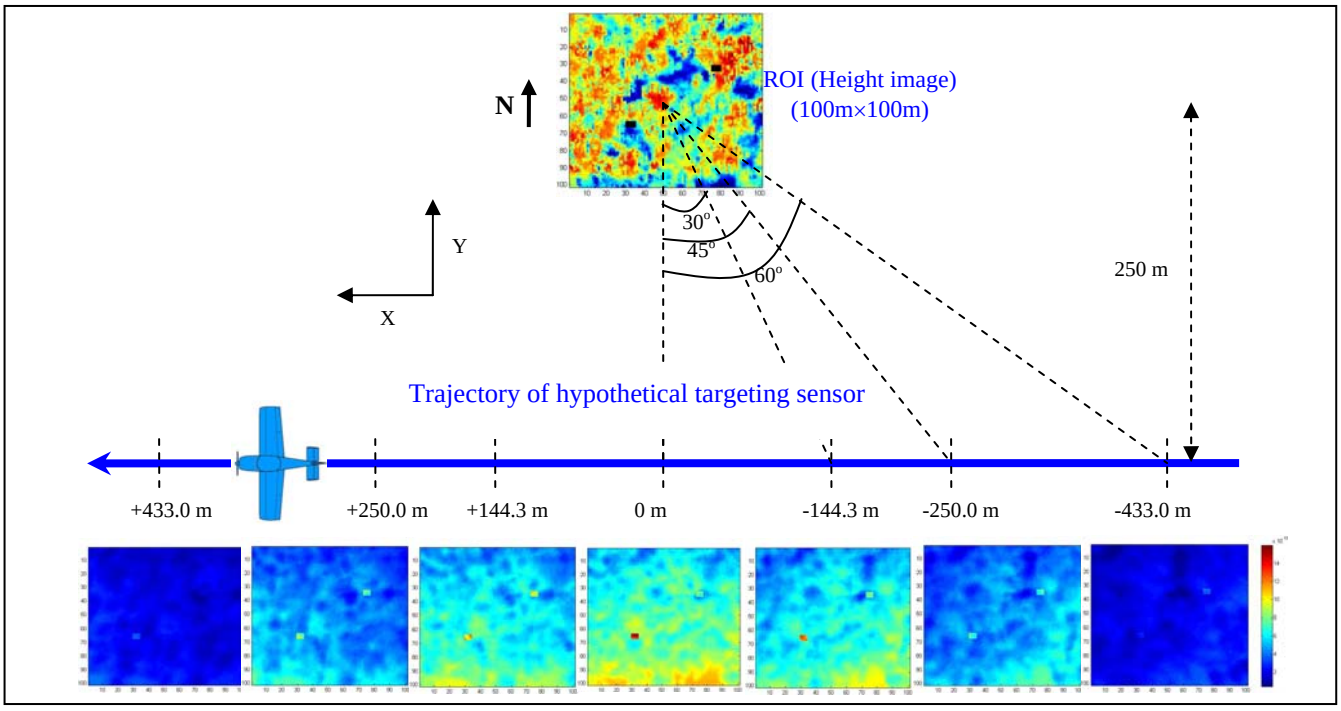

Fig. 9 A 100 m × 100 m region of interest is shown at top depicting the above-ground tree heights (same as Fig. 5). Elevations range from zero (dark blue) to approximately 30 m (red). (Bottom row) The received power maps in watts, using (11) for a hypothetical L-band radar sensor flying at 500 m AGL, with the same targets as in Fig. 8. Relative target detectability can be seen to vary with both the targeting sensor location and local clutter.